Is the near–spherical shape the "new black" for smoke?

Anna Gialitaki[1,2], Alexandra Tsekeri[1], Vassilis Amiridis[1], Romain Ceolato[3], Lucas Paulien[3], Anna Kampouri[1,2], Antonis Gkikas[1], Stavros Solomos[1], Eleni Marinou[4,1], Moritz Haarig[5], Holger Baars[5], Albert Ansmann[5], Tatyana Lapyonok[6], Anton Lopatin[7], Oleg Dubovik[6], Silke Groß[4], Martin Wirth[4] and Dimitris Balis[2]

[1] National Observatory of Athens / IAASARS, Athens, Greece
[2] Laboratory of Atmospheric Physics, Physics Department, Aristotle University of Thessaloniki, Greece
[3] ONERA, The French Aerospace Lab, Toulouse, France
[4] Institute of Atmospheric Physics, German Aerospace Center (DLR), Oberpfaffenhofen, Germany
[5] Leibniz Institute for Tropospheric Research (TROPOS), Leipzig, Germany
[6] Laboratoire d'Optique Atmosphérique, CNRS/Université Lille, Villeneuve d'Ascq, France
[7] GRASP-SAS, Villeneuve d'Ascq, France

Correspondence to: Anna Gialitaki (togialitaki@noa.gr)

Abstract. We examine the capability of near-spherical-shaped particles to reproduce the non-typical Particle Linear Depolarization Ratio (PLDR) values measured over Europe for stratospheric smoke originating from Canadian wildfires. The smoke layers were detected both in the troposphere and the stratosphere, though in the latter case the particles presented PLDR values of almost 18% at 532 nm as well as a strong spectral dependence from the UV to the Near-IR. The assumption that the smoke particles have a near-spherical shape allows for the reproduction of the observed PLDR and Lidar Ratio (LR), whereas this was not possible when using more complicated shapes. The results presented here are supported by recent findings in the literature, showing that up to now the near-spherical shape (or closely similar shapes) is the only morphology found capable of reproducing the observed intensive optical properties of stratospheric smoke, as well as their spectral dependence.

1 Introduction

Particles originating from biomass burning activities are known to have a significant effect on radiation and climate (Kaufman et al., 2002). The factors affecting the optical properties of smoke, i.e. their scattering and absorption efficiency, are mainly the black carbon fraction and the impact of the ageing processes (Amiridis et al., 2009). Various findings from field measurements suggest that the smoke particles' surface may serve as highly effective cloud nuclei (Hoose & Möhler, 2012; Marinou et al., 2019; Nichman et al., 2019), modifying cloud properties and lifetime and thus indirectly affecting the radiative budget. Their various impacts depend also on their lifetime, since they tend to alternate their properties i.e. become less absorbing or more hydrophilic due to atmospheric processes/ageing (Amiridis et al., 2009; Adachi and Buseck, 2011).

Lidars provide valuable measurements for monitoring the properties of smoke, such as the depolarization of the backscattered light that is used here to derive new information for the smoke particle shape. On a first level, the PLDR provides information about the particle non-sphericity, since spherical particles do not depolarize the backscattered light. Moreover, numerus studies have shown that the PLDR of smoke presents a large variability related to the age of the particles (Baars et al., 2019), the

5   presence of other aerosol types found inside the smoke layers (Tesche et al., 2009; Groß et al., 2011) or even the particle water uptake due to different humidity conditions (Cheng et al., 2014). These processes alter smoke particle shape, size and composition and as a result PLDR values for aged and fresh smoke may vary from 2 to 10% at 532 nm. These values can be even lower/higher in cases of mixtures with low/high depolarizing components, respectively (i.e. marine/dust particles). Müller et al. (2007) carried out an extensive study on the optical properties and the effect of atmospheric ageing of long-range-

10 transported smoke from Siberia and Canada and found that PLDR values did not exceed 1–3 % at 532 nm for 10-day-old plumes. This is comparable to findings by Nicolae et al. (2013), showing that smoke plumes up to 4-day-old present PLDR values of almost 4% at 532 nm. Moreover, measurements conducted in South Africa (Giannakaki et al., 2016) showed that for pure smoke the PLDR values at 355 nm are less than 6%. On the other hand, smoke PLDR has been found to reach values up to 12–14 % at 532 nm if significant concentrations of highly depolarizing components (i.e. soil or dust particles) exist inside

15 lofted smoke layers (Tesche et al., 2009; Veselovskii et al., 2016).

Lately, there have been observational evidence of smoke originating from large scale fires with PLDR values that exceed the typical range. For example, in Sugimoto et al. (2010) values of 12–15 % at 532 nm are presented for both tropospheric and stratospheric smoke plumes reaching from Mongolia to Nagasaki and Tsukuba in 2007. Nisantzi et al. (2014) reported values of 9–18 % at 532 nm for smoke originating from Turkish fires and observed above Cyprus after 1 to 4 days of transport. A

20 spectral dependence of smoke PLDR with decreasing values from UV to Near-IR was presented for the first time by Burton et al. (2015). The measurements were performed above Denver, Colorado with an airborne HSRL instrument during the DISCOVER-AQ (Deriving Information on Surface Conditions from Column and Vertically Resolved Observations Relevant to Air Quality) field mission. This particular smoke plume was found at 8 km height, originating from Pacific Northwest wildfires and exhibited PLDR values of 20%, 9.3% and 1.8 % at 355, 532 and 1064 nm, respectively. Implications for

25 enrichment of smoke plumes with dust particles during the emission have been reported, a process that could justify the high depolarization values recorded for tropospheric smoke (e.g. in Nisantzi et al., 2014).

In the spotlight of the large scale Canadian fires of 2017, the discussion regarding the unique feature of high PLDR values and spectral dependence for smoke has been opened also for stratospheric smoke. These wildfires inserted large amounts of smoke to the lower stratosphere by explosive Pyro-cumulonimbus activity (Khaykin et al., 2018). In fact, the smoke load in the

30 stratosphere was found to be comparable to that of a moderate volcanic eruption (Peterson et al., 2018). The smoke plumes circled the Northern hemisphere in nearly 20 days, reaching Europe in less than 10 days. Above Europe, their properties were intensively studied by the European Aerosol Research Lidar Network (EARLINET; Pappalardo et al., 2014). Multi-wavelength

lidar measurements in Central (Ansmann et al., 2018; Q. Hu et al., 2019) and South Europe (Gialitaki et al., 2019; Sicard et al., 2019) revealed high PLDR values at 355 and 532 nm and a strong spectral dependence from the UV to the Near-IR. However, despite of the extensive analysis of this event, the microphysical characterization of the stratospheric smoke particles is not yet adequate and further analysis is imperative to draw conclusions. Most of the microphysical properties reported for

5   the stratosphere are retrieved from lidar measurements using inversion algorithms and assumed scattering models that are applied in EARLINET (e.g. Veselovskii et al., 2002; Dubovik et al., 2006). For example, the derived microphysical properties presented in Haarig et al. (2018) and Hu et al. (2019) are based on the lidar backscatter and extinction coefficient profiles that were used as inputs to inversion schemes. However, the observed unusual PLDR values could not be reproduced by these studies due to the assumed shapes.

10 In our analysis, we aim to seek for an explanation that could justify the high values and non-typical spectral dependence of smoke PLDR and estimate the particle microphysical properties (i.e. shape, size and refractive index) that reproduce the measurements of both smoke PLDR and the LR at the measured wavelengths of 355, 532 and 1064 nm. The starting point and main assumption of our investigation is the particle near-spherical-shape that can be highly depolarizing as shown in the work of Mishchenko and Hovenier (1995); Mishchenko et al. (2016); Bi et al. (2018) and Ishimoto et al. (2019).

15 Our paper is organized as follows: in Sect. 2 we discuss the methodology followed for the retrieval of stratospheric smoke microphysical properties using the PLDR and LR measurements and assuming (a) near-spherical shape, as well as (b) more complicated shapes for the particles. In Sect. 3 we provide a brief description of the Canadian wildfires during August 2017, describing the mechanism that introduced the smoke particles into the lower stratosphere and the route of the smoke plume from Canada to Europe. Also the lidar measurements performed over Leipzig, Germany are included in this Section. In Sect.4

20 we present the results of our microphysical retrieval. The discussion of these results including implications on the physical process that may led to these observations and the future perspectives of our work are found in Sect. 5. Conclusions are summarized in Sect. 6.

2 Methodology

For the retrieval of the smoke microphysical properties we constructed appropriate look-up-tables using a range of particle

25 shapes, size distributions and refractive indices as described in the forthcoming sections 2.1-2.3, for near-spherical, Chebyshev and fractal shapes respectively (Fig.1). For the construction of the look-up-tables we used the T-matrix code (Mackowski and Mishchenko, 1996; Mishchenko & Travis, 1998; Mackowski & Mishchenko, 2011). The T-matrix outputs are used to calculate PLDR and LR as shown in Eq. (1) and (2):

$$\text{PLDR}\,(\lambda) = \frac{F_{11}(180°) - F_{22}(180°)}{F_{11}(180°) + F_{22}(180°)} \qquad (1)$$

$$\text{LR} (\lambda) = \frac{4\pi \, C_{ext}(\lambda)}{C_{sca}(\lambda) \, F_{11}(180°)} \tag{2}$$

where F_{ij} are the elements of the scattering matrix, C_{ext} and C_{sca} are the extinction and scattering cross sections, and λ is the wavelength (Fig. 1).

2.1 Near - spherical shapes

5 We modelled the near-spherical shapes using spheroid particles with different axial ratios ε. The axial ratio of a spheroid is defined as the ratio of the ellipse rotational axis (a) to the axis perpendicular to the rotational axis (b) as $\varepsilon = {}^{a}\!/_{b}$. If $\varepsilon > 1$ then the spheroid is characterized as prolate, whereas if $\varepsilon < 1$, the spheroid is characterized as oblate (Mishchenko et al., 2002; Dubovik et al., 2006). To describe the spheroidal shape in the spherical coordinate system we use Eq. (3) where r is the radius of the volume equivalent sphere and θ, φ are the zenith and azimuth angles respectively.

$$r(\theta,\varphi) = a \left[\sin^2\theta + \frac{a^2}{b^2} \cos^2\theta \right]^{-1/2} \tag{3}$$

For the present study we used ε values from 0.6 to 1.55. Figure 2 presents some examples of the near-spherical shapes used, embedded in a perfectly spherical shell to demonstrate their deviation from the perfect sphere.

We assumed that the shape distribution of the near-spherical particles is a mono-modal, normal distribution $n_s(\varepsilon)$ as
15 shown in Eq. (4), with σ_s the sigma of the distribution fixed to 0.05, and ε_s the mean axial ratio (Table 1). We also assume that the shape distribution does not change with particle size.

$$n_s(\varepsilon) = \frac{1}{\sqrt{2\pi}\,\sigma_s} \exp\left(-\frac{(\varepsilon - \varepsilon_s)}{2\sigma_s^{\,2}} \right) \tag{4}$$

The size distributions considered for the near-spherical particles are mono-modal and log-normal with mean geometric radius r_g, and geometric standard deviation σ_g , as shown in Eq. (5). The grid used for r_g is $0.1 - 0.7$ μm, while σ_g
20 is fixed at 0.4.Maximum and minimum radius of the distribution are $r_{min} = 0.001$ and $r_{max} = 2$ μm respectively.

$$n(r) = \frac{1}{\sqrt{2\pi}\,r\,\sigma_g} \exp\left[-\frac{1}{2}\left(\frac{\ln(r/r_g)}{\sigma_g} \right)^2 \right] \tag{5}$$

We used a wavelength-independent refractive index k with real part (m_r) varying from 1.4 to 1.75 and imaginary part (m_i) varying from 0.005 to 0.05 (Müller et al., 2005; Nicolae et al., 2013; Giannakaki et al., 2016). An overview of the values used for the generation of the look-up-tables for the near-spherical particles is presented in Table 1.

2.2 Chebyshev particles

In order to investigate whether particles of more complicated shapes than the near-spherical shape can reproduce both the PLDR and LR measurements of stratospheric smoke, we constructed look-up-tables for smoke particles resembling "Chebyshev particles" using the T-matrix code. Chebyshev particles (Fig. 3 in Mishchenko and Travis, 1998) are produced by the deformation of a sphere by means of a Chebyshev polynomial. In the spherical coordinates system, their shape is described as shown in Eq. (6), where r_0 is the radius of the perfect sphere, u is the deformation parameter and $T_n(cos\theta)$ is the Chebyshev polynomial of degree n (Mishchenko and Travis, 1998).

$$r(\theta,\varphi) = r_0(1 + u\,T_n(cos\theta)), \quad |u|<1 \tag{6}$$

Only Chebyshev polynomials of fourth degree were used, with deformation parameter values of $u = \pm 0.05$ to ± 0.15. We considered the same refractive indices as the ones used for the generation of the look-up-tables of the near-spherical particles, while for the size distribution we used also mono-modal, log-normal distributions. Table 2 summarizes the properties chosen for the Chebyshev particles.

2.3 Fractal morphology

Scattering calculations for highly-irregular soot aggregates with a chain-like fractal morphology have been also included in our study (Fig. 3). These fractals are selected such as to account for the possibility that initially emitted chain-like aggregates (Martins et al., 1998; Zhang et al., 2008; Chakrabarty et al., 2014), are injected in the stratosphere and sustained their shape. A physical process that could be responsible for such an injection could be the abrupt upward motions inside the Pyro-cumulonimbus cloud, resulting in limited interaction of the particles with other tropospheric constituents.

The geometry of soot aggregates is provided by the Tunable Cluster Aggregation (TCA) code (Mackwoski, 1995; 2006). The parameters that characterize the morphology of the particles is the fractal pre-factor k_f, the fractal dimension D_f, the number of monomers N that cluster to form the aggregate, the monomer radius r_m and the gyration radius R_g (i.e. the overall aggregate radius), following the power-law relationship of Eq.(7) (Liu & Mishchenko, 2018).

$$N = k_f \left(\frac{R_g}{r_m}\right)^{D_f} \tag{7}$$

The scattering properties of the fractals are calculated by means of the Multi-Sphere T-Matrix code (MSTM) (Mackowski and Mishchenko, 2011), with typical values for the density, which depends on fractal dimension and fractal pre-factor. We specifically use the values of $D_f = 1.8$ and $k_f = 1.3$ corresponding to values reported for fractals emitted from large-scale fires (Kahnert et al., 2012; Ceolato et al., 2018). To account for different fractal morphologies we use a range of monomer number

5   N = 244, 579 and 1953 with monomer radius r_m = 40, 60 and 80 nm, correspondingly (Fig. 3). Monomer number and radius were chosen so that the volume equivalent radius R_v is equal to 500 nm. The refractive index values used are k = (1.4, 1.45, 1.5) + i(0.005, 0.01, 0.03). Table 3 summarizes the properties chosen for the chain-like fractal particles.

3 Description of the dispersion and vertical distribution of smoke

The extreme pyro-convection (Fromm et al., 2010) that was recorded in the area of British Columbia (western Canada) during

10   summer 2017, resulted in particularly strong updrafts that penetrated and released large amounts of smoke particles into the lower stratosphere (Peterson et al., 2018). Here we use an ensemble of satellite observations from MODIS (Moderate Resolution Imaging Spectroradiometer) on board Terra and Aqua, OMPS (Ozone Mapping and Profiler Suite) on board Suomi NPP and CALIOP (Cloud-Aerosol Lidar with Orthogonal Polarization) on board CALIPSO, to identify the dispersion and vertical distribution of the plume above Canada, as well as the profile of PLDR at 532 nm from CALIOP. The combination of

15   these observations is shown in Fig. 4, where true-color images from MODIS are overlaid with the fire active regions and thermal anomalies (red dots) from Suomi NPP and CALIPSO (yellow lines) overpasses on 8 and 15 August 2017, when the smoke plume has already reached Europe. Figures 5 and 6 show the Backscatter Coefficient and PLDR curtain plots at 532 nm from CALIPSO measurements. Based on these observations smoke plumes were found above the regions of fire activity since the beginning of August (Fig. 4a), when the plumes remained in the troposphere, below 5-6 km (39º – 45º N, 123º – 125º

20   W) (Fig. 5a, red dashed lines), exhibiting low PLDR values of the order of 3 – 4 % (Fig. 5b). Then on August 12, the unprecedented buoyancy force caused by the strong fire activity started lifting the plumes up towards the tropopause, while already on August 15 smoke covered a large part of North Canada (Fig. 4b). CALIPSO observations on August 12 reveal that the plume is injected into the stratosphere at almost 13 km height (63º – 69º N, 89º – 94º W) (Fig. 6a, red dashed lines) and PLDR values exceed 15% at 532 nm (Fig. 6b). Inside the lower stratosphere, unaffected by the intensive tropospheric

25   interactions, smoke particles started drifting, following a North-Easterly direction and first appeared over Europe approximately after mid-August.

Interestingly, even after two months of the initial stratospheric smoke injection the plume seems to have sustained its high depolarization capability. Specifically, airborne lidar measurements performed above the Atlantic showed PLDR values in the range of 10 – 14 % between 10 and 12 km (Fig. 7a) near the west coast of Ireland (Fig. 7c). These observations were

30   conducted in the framework of Wave-driven ISentropic Exchange (WISE) mission organised by the German Aerospace Centre

(DLR) and support the high depolarization values detected for months over Europe by EARLINET, as shown in Fig. 7 in Baars et al. (2019).

3.1 Lidar measurements in Leipzig

The highest smoke load over EARLINET stations has been reported at Leipzig, Germany (Ansmann et al., 2018; Baars et al., 2019). Measurements at the Leibniz Institute of Tropospheric Research (TROPOS) were conducted with the BERTHA (Backscatter Extinction lidar-Ratio Temperature Humidity profiling Apparatus) multi-wavelength polarization Raman lidar system. The system measures the total and cross-polarized component of the elastic backscattered light at 355, 532 and 1064 nm, which are used to derive the PLDR at these wavelengths. It is also able to perform independent measurements of the aerosol extinction coefficient at 387, 607 nm and (after optics re-arrangement) at 1058 nm, and thus has a capability to provide the LR profiles at 355, 532 and 1064 nm (Haarig et al., 2017). On August 22, the profiles of the stratospheric smoke backscatter and extinction coefficients at 355, 532 and 1064 nm and the smoke PLDR at 355 and 532 nm were derived from two-and-a-half-hour averaging of the lidar signals between 20:45 and 23:17 UTC. The PLDR value at 1064 nm was calculated using a forty-minute averaging between 23:50 and 00:30 UTC (Haarig et al., 2018). The gap between the end of the first measurement and the beginning of the second, corresponds to the necessary time for the rearrangement of BERTHA optics.

Layer-integrated values of PLDR and LR for the stratospheric smoke layer are calculated in Haarig et al. (2018) and shown in Fig. 8 and Table 4 along with their errors. The derived LRs are typical for aged Canadian smoke at 355 nm (40 ± 16 sr) and 532nm (66 ± 12 sr) (Müller et al., 2007). Low signal-to-noise ratio at the plume height prevented detailed retrievals of particle extinction coefficient at 1058 nm. Thus, for the LR values at 1064 nm only few measurement points could be derived (Haarig et al., 2018). This yields a LR value of 92 ± 27 sr at 1064 nm. The increasing tendency of the LR from the UV to the visible part of the spectrum has been also reported before for aged Canadian smoke (Müller et al., 2007), advocating to a possible increase at the Near-IR, although this is not currently supported by other observational evidence found in the literature. On the other hand, the PLDR values are far from typical for aged smoke. The layer-integrated PLDR value at 355 nm is 22 ± 2 %, decreasing to 18 ± 1 % at 532 nm and 4 ± 0.8 % at 1064 nm. These results are in agreement with the PLDR values measured above Lille and Palaiseu from August 24 to 28, 2017 (Hu et al., 2019).

4 Smoke microphysical retrieval

4.1 Near – spherical particles

First, we present the smoke microphysical retrieval considering the near-spherical shape for the smoke particles, as described in section 2.2. The search in the T-matrix look-up tables is performed on the basis of achieving the minimum sum of squares of relative differences between measurements and simulations as shown in, Eq. (8) (see also Fig. 1).

$$\sum_{i=1}^{n} \left(\frac{M_\lambda^i - S_\lambda^i}{M_\lambda^i}\right)^2 = min \qquad (8)$$

Where M_λ^i denotes to measured PLDR and LR at wavelength λ = 355, 532 and 1064 nm and S_λ^i denotes to the corresponding simulations. Out of the results, the solution is accepted based on the requirement that each simulated value has to be within the measurement error (Eq. 9).

$$S_\lambda^i \leq e(M_\lambda^i) \qquad (9)$$

This minimization is achieved for near-spherical particles with mean axial ratio ε_s = 1.4 (Fig.9), complex refractive index k = 1.55 + i0.025 and mean geometric radius r_g = 0.25μm (Fig. 10). The fitting of the measurements is presented in Fig. 11 and Table 5 along with the relative difference with respect to the measured mean values. The latter are within the measurement

10 errors (Table 4).

Figure 10 presents also a comparison of the retrieved size distribution with respect to the size distribution provided for biomass burning originating from Boreal forest in AERONET climatology in Dubovik et al. (2002). What is interesting here is that the retrieved sizes for near-spherical smoke particles are absent in the AERONET climatology product. This is could be attributed either to the in-frequent presence of near-spherical smoke particles, or to the absence of near-spherical particles in the shape

15 distribution used for non-spherical particles in the AERONET retrieval (see Fig. 11b of Dubovik et al., 2006).

4.2 Chebyshev particles

For Chebyshev particles of fourth degree (T_4) used here, the search in the constructed look-up-tables did not produce a successful fitting of the measurements (Fig. 12). Specifically, the PLDR values at 532 nm deviate from the measured values.

20 Table 6 presents indicatively the results that provided the minimum relative difference with respect to the measured mean values.

4.3 Fractal aggregates

Results for fractal aggregates are shown in Fig.13 and Table 7. By increasing monomer radius, we manage to increase significantly the PLDR values at all wavelengths but still fail to reproduce the measurements. As shown in Ishimoto et al.

25 (2019), in order to reproduce the PLDR and LR measurements for aged smoke particles the fractals need to be coated by other material, producing a shape that closely resembles the near-spherical shape (i.e. shapes of "Type-B, size 11, Vr = 20" shown

in Fig. 4 of Ishimoto et al. 2019). Table 7 presents the PLDR and LR values for fractals with $R_m = 80\mu m$, which produced the results closest to the measured values, for different refractive indices.

5 Discussion

The use of near-spherical shapes is found to well-reproduce the measurements of smoke optical properties, as well as their wavelength dependence. The near-spherical model presented here could be valuable for operational retrievals, e.g. the AERONET operational aerosol retrieval (Dubovik et al., 2006), since it provides a much simpler and faster solution with respect to more complicated shapes (e.g. Mishchenko et al.,2016; Ishimoto et al., 2019). The non-spherical particles in the AERONET retrieval scheme are optimized for dust and they are modelled as spheroids with axial ratios smaller than 0.7 and larger than 1.4 (Fig. 11b in Dubovik et al. 2006), thus omitting the near-spherical particles. The extension of the AERONET scattering model to include the near-spherical shapes could possibly improve the retrieval in presence of near-spherical particles i.e. smoke or even some pollen species which often have near-spherical shapes (Bohlmann et al., 2019).

What is though the underlying physical process that results in near-spherical-shapes and high PLDRs for smoke? Previous studies attribute the high PLDR values to the presence of dust particles in the elevated smoke plumes, as a result of the strong convection over soils during intense fires (e,g. Sugimoto et al., 201; Dahlkoter et al., 2014; Nisantzi et al., 2014). Moreover, it has been suggested that the particles can keep their initial aggregate-like structures (Haarig et al., 2018), or that ice crystals are formed on smoke particles at high altitudes (Sicard et al., 2019). These possible processes are adequately reviewed in an extensive discussion found in Burton et al. (2015). In fact, soil lifting inside the smoke plume could explain the Leipzig PLDR observations presented in this study. However, even though the low extinction-related Angstrom exponent ($- 0.3 \pm 0.4$) observed for this case could additionally support this assumption, it is difficult to believe that coarse mode particles are injected in the stratosphere and remain there 10 days after emission. Furthermore, the computations performed herein showed that the more complex shapes assumed for smoke, in terms of surface roughness alternations or particle ensembles, were found to be inadequate in reproducing the PLDR and LR values for stratospheric smoke, while also the high values of LR measured (see section 3.1) advocate dissuasive towards ice formation. Moreover, Liu and Mishchenko (2019) showed that the multi-wavelength PLDR measurements of Burton et al. (2015) can be reproduced assuming spherical tar ball aggregates inside the smoke plume. However, the tar ball morphologies considered in the study of Liu and Mishchenko (2019) do not fit the PLDR observations presented herein, while up to now the LR values are not reproduced either.

For our study we would like to promote another perspective on the physical process that could justify the presence of near-spherical particles inside the stratospheric smoke plume. This process is reported by laboratory experiments (Zhang et al. 2008), where the behavior of smoke aggregates after exposure to sulfuric acid (H_2SO_4) vapor was analyzed. In particular, freshly emitted soot particles that initially had a chain-like agglomerate structure, consisting of rather small monomers (~15μm in diameter), shrank and collapsed to a compact near-spherical form after exposure to ~3μgr/m³ sub-saturated H_2SO_4 vapor

(Fig.1 in Zhang et al., 2008). The samples of soot collected after the exposure had a sulfuric acid coating formed around them, while a superposition of the optical properties of the two different aerosol types was observed. The hydroscopic mobility size growth (D) and hydroscopic mass growth (M) of the coated particles was afterwards investigated under different relative humidity (RH) conditions. Thought M increased with increasing RH for all initial agglomerates sizes used (of 50, 155 and 245

5   nm in diameter), the larger the initial agglomerate size, the higher RH (>50%) values were needed in order for particles to collapse to a compact, nearly-spherical form and then start growing by water condensation (Zhang et al., 2008).

These results led us to the hypothesis that in order to have a complete shape reconstruction of smoke towards a nearly spherical compact form, two criteria need to be fulfilled: (a) sufficient sulfate aerosol concentrations that can be achieved either by (i) the SO_2 (H_2SO_4 precursor) released during by the large scale fire itself or (ii) provided by an external source, and (b) favorable

10   RH conditions (an unsaturated environment). Regarding the RH stratospheric levels needed to reproduce laboratory conditions, a recent study by Yu et al. (2019) reported increased water vapor values in the Upper Troposphere - Lower Stratosphere (UTLS), at the injection height of the smoke plume due to the strong convection by the Pyro-cumulonimbus. Water vapor observations by the Microwave Limb Sounder (EOS-MLS, Fig. 14) support that the RH conditions needed were likely met, due to the Pyro-cumulonimbus eruption that injected water-vapor-rich air masses to the stratosphere.

15   Furthermore, observational evidence from satellite imagery reveal that the days preceding the Pyro-cumulonimbus event increased volcanic activity of Shiveluch Volcano in Kamchatka Peninsula (56.65 N, 161.36 E) was recorded on a daily basis (https://ds.data.jma.go.jp/svd/vaac/data/Archives/2017_vaac_list.html), while on August 8 a large ash cloud was lifted up to 10 km (https://volcano.si.edu/volcano.cfm?vn=300270&vtab=Weekly#August2017, https://watchers.news/2017/08/09/sheve luch-eruption-russia-august-2017/). Figure 15a shows the True-Color image from MODIS on that day, overlaid with the UTLS

20   SO_2 concentration product from Suomi NPP (blue colour). Here, we can identify the plume that drifts south-east towards the area of British Columbia, which is also visible on the satellite images from Himawari-8 (Fig. 15b).

The aforementioned observations provide an indication that the two air masses carrying smoke and H_2SO_4 particles may have crossed along their track, and due to the favorable RH conditions prevailing in the UTLS at the time (significantly different than the troposphere), resulted in substantially restructured coated soot particles that resemble near-spherical shapes. Our

25   ongoing research investigates whether this concurrence, or the large amounts of SO_2 "internally" released by the fire, or even the stratospheric sulfate background already pre-existing at the stratospheric smoke injection height, is the reason behind the unique large values of stratospheric PLDR. The months following the event, particles in the stratosphere seem to have slowly lost their high depolarizing capability (Baars et al., 2019). This could possibly be due to gravitational settling removing larger coated soot particles, evaporation of the volatile H_2SO_4 from the surface of smoke particles, or even due to the fact that under

30   the dry stratospheric conditions the initially high RH values could not be preserved.

6 Conclusions

The unique optical properties of transported stratospheric smoke, originating from the Pyro-cumulonimbus activity of the large Canadian fires 2017, were reproduced using T-matrix simulations and assuming near-spherical shapes for smoke. This is consistent with results of past studies showing that near-spherical particles produce PLDR values that can reach up to 100%

5 depending also on their size and composition (Bi et al., 2018) and that smoke particles in particular, when coated with weakly absorbing materials and resemble near-spherical shapes, can produce large depolarization with a noticeable spectral dependence (Mishchenko et al. 2016; Ishimoto et al., 2019). Furthermore, our analysis showed that the more complicated morphologies considered herein cannot reproduce the measurements. As a next step and to provide a possible explanation on the strong smoke PLDR, we propose a simple idea based on laboratory experiments: if smoke plumes lifted to UTLS region

10 coexist with particles of sulfuric nature then, under sub-saturated conditions, smoke particle shape changes and collapses into a near-spherical compact form. The validation of this hypothesis is part of our forthcoming research. Concluding, studying the stratospheric smoke from the Canadian wildfire activity provide us with the great opportunity of showing the remote sensing value and the need for coordinated ground-based lidar network measurements such as EARLINET, as an exploratory tool in investigating unknown processes in the stratosphere.

15 *Author contributions.* VA, AT and AG conceived the presented idea; VA and AT supported AG on the analysis, manuscript preparation, and figures design; AT guided and supervised AG on the scattering model calculations and results interpretation; RC and LP performed the analysis on fractal aggregates scattering properties and provided AG with the results; AG, AK and SS analysed the MLS water vapour data and performed Flexpart model runs to support the dispersion of the smoke and volcanic plumes (not shown in the final manuscript); EM prepared the CALIPSO data and figures; MH, HB and AA collected and

20 analysed Leipzig lidar measurements; TL, AL and OD supported AG to confirm T-matrix results for near-spherical particles; SG and MW performed the airborne lidar measurements and the corresponding analysis; DB advised AG on the interpretation of the results of this study. All authors provided critical feedback and helped shape the research, analysis and manuscript.

Competing interests. The authors declare that they have no conflict of interest.

Special issue statement. This article is part of the special issue "EARLINET aerosol profiling: contributions to atmospheric and climate research". It is not associated with a conference.

30 *Acknowledgements.* We are grateful to EARLINET (https://www.earlinet.org/, last access: 10 January 2020), ACTRIS (https://www.actris.eu, last access: 10 January 2020), for the data collection, calibration, processing and dissemination. We are grateful to the AERIS/ICARE Data and Services Center for providing access to the CALIPSO data used and their

computational center (http: //www.icare.univ-lille1.fr/, last access: 10 January 2020). We thank the NASA/LaRC/ASDC for making available the CALIPSO products. We acknowledge the use of imagery from the Worldview Snapshots application (https://wvs.earthdata.nasa.gov/, last access: 10 January 2020), part of the Earth Observing System Data and Information System (EOSDIS). The authors are grateful to the NASA EOS Aura MLS team for providing free access to the MLS water

5 vapour data (https://mls.jpl.nasa.gov/products/h2o_product.php/, last access: 10 January 2020). The authors would like to acknowledge the Tokyo VAAC (https://ds.data.jma.go.jp/svd/vaac/data/index.html, last access: 10 January 2020) for making Volcanic Ash Advisories archives freely available.

Financial support. The research leading to these results was supported through the European Research Council (ERC) under

10 the European Community's Horizon 2020 research and innovation framework program – ERC grant agreement 725698 (D-TECT). Anna Gialitaki acknowledges support of this work by the project "PANhellenic infrastructure for Atmospheric Composition and climatE chAnge" (MIS 5021516), which is implemented under the action "Reinforcement of the Research and Innovation Infrastructure", funded by the operational program "Competitiveness, Entrepreneurship and Innovation" (NSRF 2014–2020) and co-financed by Greece and the European Union (European Regional Development Fund). NOA team

15 acknowledges the support of Stavros Niarchos Foundation (SNF).

References

Adachi, K., and Buseck, P. R.: Atmospheric tar balls from biomass burning in Mexico, J. Geophys. Res.-Atmos., 116, D05204, https://doi.org/10.1029/2010JD015102, 2011.

Amiridis, V., Balis, D. S., Giannakaki, E., Stohl, A., Kazadzis, S., Koukouli, M. E., and Zanis, P.: Optical characteristics of

20 biomass burning aerosols over Southeastern Europe determined from UV-Raman lidar measurements, Atmos. Chem. Phys., 9, 2431–2440. https://doi.org/10.5194/acp-9-2431-2009, 2009.

Ansmann, A., Baars, H., Chudnovsky, A., Mattis, I., Veselovskii, I., Haarig, M., Seifert, P., Engelmann, R., Wandinger, U.: Extreme levels of Canadian wildfire smoke in the stratosphere over central Europe on 21-22 August 2017, Atmos. Chem. Phys., 18, 11831–11845. https://doi.org/10.5194/acp-18-11831-2018, 2018.

25 Baars, H., Ansmann, A., Ohneiser, K., Haarig, M., Engelmann, R., Althausen, D., Hanssen, I., Gausa, M., Pietruczuk, A., Szkop, A., Stachlewska, I. S., Wang, D., Reichardt, J., Skupin, A., Mattis, I., Trickl, T., Vogelmann, H., Navas-Guzmán, F., Haefele, A., Acheson, K., Ruth, A. A., Tatarov, B., Müller, D., Hu, Q., Podvin, T., Goloub, P., Veselovskii, I., Pietras, C., Haeffelin, M., Fréville, P., Sicard, M., Comerón, A., Fernández García, A. J., Molero Menéndez, F., Córdoba-Jabonero, C., Guerrero-Rascado, J. L., Alados-Arboledas, L., Bortoli, D., Costa, M. J., Dionisi, D., Liberti, G. L., Wang,

30 X., Sannino, A., Papagiannopoulos, N., Boselli, A., Mona, L., D'Amico, G., Romano, S., Perrone, M. R., Belegante, L., Nicolae, D., Grigorov, I., Gialitaki, A., Amiridis, V., Soupiona, O., Papayannis, A., Mamouri, R.-E., Nisantzi, A., Heese,

B., Hofer, J., Schechner, Y. Y., Wandinger, U., and Pappalardo, G.: The unprecedented 2017–2018 stratospheric smoke event: decay phase and aerosol properties observed with the EARLINET, Atmos. Chem. Phys., 19, 15183–15198, https://doi.org/10.5194/acp-19-15183-2019, 2019.

Bohlmann, S., Shang, X., Giannakaki, E., Filioglou, M., Saarto, A., Romakkaniemi, S., and Komppula, M.: Detection and characterization of birch pollen in the atmosphere using a multiwavelength Raman polarization lidar and Hirst-type pollen sampler in Finland, Atmos. Chem. Phys., 19, 14559–14569, https://doi.org/10.5194/acp-19-14559-2019, 2019.

Bi, L., Lin, W., Liu, D., and Zhang, K.: Assessing the depolarization capabilities of nonspherical particles in a super-ellipsoidal shape space, Opt. Express, 26, 1726–1742. https://doi.org/10.1364/OE.26.001726, 2018.

Burton, S. P., Hair, J. W., Kahnert, M., Ferrare, R. A., Hostetler, C. A., Cook, A. L., Harper, D. B., Berkoff, T. A., Seaman, S. T., Collins, J. E., Fenn, M. A., and Rogers, R. R.: Observations of the spectral dependence of linear particle depolarization ratio of aerosols using NASA Langley airborne High Spectral Resolution Lidar, Atmos. Chem. Phys., 15, 13453–13473, https://doi.org/10.5194/acp-15-13453-2015, 2015.

Ceolato, R., Gaudfrin, F., Pujol, O., Riviere, N., Berg, M. J., & Sorensen, C. M.: Lidar cross-sections of soot fractal aggregates: Assessment of equivalent-sphere models., J. Quant. Spectrosc. Ra., 212, 39–44. https://doi.org/10.1016/j.jqsrt.2017.12.004, 2018.

Chakrabarty, R.K., Beres, N.D., Moosmüller, H., China, S., Mazzoleni, C., Dubey, M.K., Liu, L., Mishchenko, M.I.: Soot superaggregates from flaming wildfires and their direct radiative forcing, Scientific Reports, 4. https://doi.org/10.1038/srep05508, 2014.

Cheng, T., Gu, X., Wu, Y., Chen, H.: Effects of atmospheric water on the optical properties of soot aerosols with different mixing states, J. Quant. Spectrosc. Ra, 147, 196-206, https://doi.org/10.1016/j.jqsrt.2014.06.002, 2014.

Dahlkötter, F., Gysel, M., Sauer, D., Minikin, A., Baumann, R., Seifert, P., Ansmann, A., Fromm, M., Voigt, C., and Weinzierl, B.: The Pagami Creek smoke plume after long-range transport to the upper troposphere over Europe–aerosol properties and black carbon mixing state, Atmospheric Chemistry and Physics, 14, 6111–6137, 2014

Dubovik, O., Holben, B., Eck, T. F., Smirnov, A., Kaufman, Y. J., King, M. D., Tanré, D., and Slutsker, I.: Variability of absorption and optical properties of key aerosol types observed in worldwide locations, Journal of the atmospheric sciences, 59, 590–608, 2002.

Dubovik, O., Sinyuk, A., Lapyonok, T., Holben, B. N., Mishchenko, M., Yang, P., Eck, T. F., Voltne, H., Munoz, O., Veihelmann, B., Van der Zande, W. J., Leon, J.-F., Sorokin, M., and Slutsker, I.: Application of spheroid models to account for aerosol particle nonsphericity in remote sensing of desert dust, J. Geophys. Res., 111, D11208, doi:10.1029/2005JD006619, 2006.

Fromm, M., Lindsey, D. T., Servranckx, R., Yue, G., Trickl, T., Sica, R., Doucet, P., and Godin-Beekmann, S. E.: The untold story of pyrocumulonimbus, B. Am. Meteorol. Soc., 91, 1193–1209, https://doi.org/10.1175/2010bams3004.1, 2010.

Gialitaki, A., Tsekeri, A., Amiridis, V., Ceolato, R., Paulien, L., Proestakis, E., Marinou, E., Haarig, M., Baars, H., and Balis, D.: Is near-spherical shape the "new black" for smoke?, in: Proceedings of the 29th International Laser Radar Conference (ILRC), Hefei, Anhui, China, 24–28 June 2019, 114–117, 2019.

Giannakaki, E., Van Zyl, P. G., Müller, D., Balis, D., and Komppula, M.: Optical and microphysical characterization of aerosol layers over South Africa by means of multi-wavelength depolarization and Raman lidar measurements, Atmos. Chem. Phys., 16, 8109–8123. https://doi.org/10.5194/acp-16-8109-2016, 2016.

Groß, S., Tesche, M., Freudenthaler, V., Toledano, C., Wiegner, M., Ansmann, A., Althausen, D., and Seefeldner, M.: Characterization of Saharan dust, marine aerosols and mixtures of biomassburning aerosols and dust by means of multi-wavelength depolarization and Raman lidar measurements during SAMUM 2, Tellus B, 63, 706–724, doi:10.1111/j.1600-0889.2011.00556.x, 2011.

Groß, S., Esselborn, M., Weinzierl, B., Wirth, M., Fix, A., & Petzold, A.: Aerosol classification by airborne high spectral resolution lidar observations, Atmos. Chem. Phys., 13, 2487–2505. https://doi.org/10.5194/acp-13-2487-2013, 2013.

Haarig, M., Ansmann, A., Althausen, D., Klepel, A., Groß, S., Freudenthaler, V., Toledano, C., Mamouri, R.-E., Farrell, D. A., Prescod, D. A., Marinou, E., Burton, S. P., Gasteiger, J., Engelmann, R., and Baars, H.: Triple-wavelength depolarization-ratio profiling of Saharan dust over Barbados during SALTRACE in 2013 and 2014, Atmos. Chem. Phys., 17, 10767–10794, https://doi.org/10.5194/acp-17-10767-2017, 2017.

Haarig, M., Ansmann, A., Baars, H., Jimenez, C., Veselovskii, I., Engelmann, R., and Althausen, D.: Depolarization and lidar ratios at 355, 532, and 1064 nm and microphysical properties of aged tropospheric and stratospheric Canadian wildfire smoke, Atmos. Chem. Phys., 18, 11847–11861, https://doi.org/10.5194/acp-18-11847-2018, 2018.

Hoose, C., and Möhler, O.: Heterogeneous ice nucleation on atmospheric aerosols: A review of results from laboratory experiments, Atmos. Chem. Phys., 12, 9817–9854. https://doi.org/10.5194/acp-12-9817-2012, 2012.

Hu, Q., Goloub, P., Veselovskii, I., Bravo-Aranda, J.-A., Popovici, I. E., Podvin, T., Haeffelin, M., Lopatin, A., Dubovik, O., Pietras, C., Huang, X., Torres, B., and Chen, C.: Long-range-transported Canadian smoke plumes in the lower stratosphere over northern France, Atmos. Chem. Phys., 19, 1173–1193, https://doi.org/10.5194/acp-19-1173-2019, 2019.

Ishimoto, H., Kudo, R., and Adachi, K.: A shape model of internally mixed soot particles derived from artificial surface tension, Atmos. Meas. Tech., 12, 107–118, https://doi.org/10.5194/amt-12-107-2019, 2019.

Kahnert, M., Nousiainen, T., Lindqvist, H., and Ebert, M.: Optical properties of light absorbing carbon aggregates mixed with sulfate: assessment of different model geometries for climate forcing calculations, Opt. Express, 20, 10042–10058, doi:10.1364/OE.20.010042, 2012.

Kaufman, Y. J., Tanré, D., and Boucher, O.: A satellite view of aerosols in the climate system. Nature, 419, 215–223. https://doi.org/10.1038/nature01091, 2002.

Khaykin, S. M., Godin-Beekmann, S., Hauchecorne, A., Pelon, J., Ravetta, F., and Keckut, P.: Stratospheric smoke with unprecedentedly high backscatter observed by lidars above southern France, Geophys. Res. Lett., 45, 1639–1646, https://doi.org/10.1002/2017GL076763, 2018.

Liu, L., & Mishchenko, M. I.: Scattering and radiative properties of morphologically complex carbonaceous aerosols: A
5   systematic modeling study. Remote Sensing, 10, https://doi.org/10.3390/rs10101634, 2018.

Liu, L., & Mishchenko, M. I.: Modeling study of scattering and absorption properties of tar-ball aggregates. Applied Optics, 58, 8648–8657. https://doi.org/10.1364/AO.58.008648, 2019.

Mackowski D. W.: Electrostatics analysis of radiative absorption by sphere clusters in the rayleigh limit: application to soot particles, Applied Optics, 343, 535–3545, 1995.

10   Mackowski, D. W., and Mishchenko, M. I.: Calculation of the T matrix and the scattering matrix for ensembles of spheres. Journal of the Optical Society of America A: Optics and Image Science, and Vision, 13, 2266–2278. https://doi.org/10.1364/JOSAA.13.002266, 1996.

Mackowski D. W.: A simplified model to predict the effects of aggregation on the absorption properties of soot particles, Journal of Quantitative Spectroscopy and Radiative Transfer, 100, 237–249, 2006.

15   Mackowski D. W., and Mishchenko M.: A multiple sphere t-matrix fortran code for use on parallel computer clusters, Journal of Quantitative Spectroscopy and Radiative Transfer, 112, 2182–219, 2011.

Marinou, E., Tesche, M., Nenes, A., Ansmann, A., Schrod, J., Mamali, D., Tsekeri, A., Pikridas, M., Baars, H., Engelmann, R., Voudouri, K.-A., Solomos, S., Sciare, J., Groß, S., Ewald, F., and Amiridis, V.: Retrieval of ice-nucleating particle concentrations from lidar observations and comparison with UAV in situ measurements, Atmos. Chem. Phys., 19,
20   11315–11342, https://doi.org/10.5194/acp-19-11315-2019, 2019.

Martins, J. V., Hobbs, P. V., Weiss, R. E., and Artaxo, P.: Sphericity and morphology of smoke particles from biomass burning in Brazil, J. Geophys. Res.-Atmos., 103, 32051–32057, doi:10.1029/98JD01153, 1998.

Mishchenko, M. I. and Hovenier, J. W.: Depolarization of light backscattered by randomly oriented nonspherical particles, Opt. Lett., 20, 1356–1358, 1995.

25   Mishchenko, M.I., and Travis, L. D.: Capabilities and limitations of a current FORTRAN implementation of the T-matrix method for randomly oriented, rotationally symmetric scatterers. J. Quant. Spectrosc. Ra., 60, 309–324. https://doi.org/10.1016/S0022-4073(98)00008-9, 1998.

Mishchenko, Michael I, Travis, L. D., and Lacis, A. A.: Scattering, absorption and emission of light by small particles. Cambridge: Cambridge University Press, 2002.

30   Mishchenko, M. I., Dlugach, J. M., and Lui, L.: Linear depolarization of lidar returns by aged smoke particles, Appl. Opt., 55, 9968–9972, https://doi.org/10.1364/AO.55.009968, 2016.

Müller, D., Mattis, I., Wandinger, U., Ansmann, A., Althausen, D., and Stohl, A.: Raman lidar observations of aged Siberian

and Canadian forest fire smoke in the free troposphere over Germany in 2003: Microphysical particle characterization, J. Geophys. Res.-Atmos., 110, D17201, doi:10.1029/2004jd005756, 2005.

Müller, D., Mattis, I., Ansmann, A., Wandinger, U., Ritter, C., and Kaiser, D.: Multiwavelength Raman lidar observations of particle growth during long-range transport of forest-fire smoke in the free troposphere, Geophys. Res. Lett., 34. https://doi.org/10.1029/2006GL027936, 2007.

Nichman, L., Wolf, M., Davidovits, P., Onasch, T. B., Zhang, Y., Worsnop, D. R., Bhandari, J., Mazzoleni, C., and Cziczo, D. J.: Laboratory study of the heterogeneous ice nucleation on black-carbon-containing aerosol, Atmos. Chem. Phys., 19, 12175–12194, https://doi.org/10.5194/acp-19-12175-2019, 2019.

Nicolae, D., Nemuc, A., Müller, D., Talianu, C., Vasilescu, J., Belegante, L., and Kolgotin, A.: Characterization of fresh and aged biomass burning events using multiwavelength Raman lidar and mass spectrometry, J. Geophys. Res.-Atmos., 118(7), 2956–2965. https://doi.org/10.1002/jgrd.50324, 2013.

Nisantzi, A., Mamouri, R. E., Ansmann, A., and Hadjimitsis, D.: Injection of mineral dust into the free troposphere during fire events observed with polarization lidar at Limassol, Cyprus, Atmos. Chem. Phys., 14, 12155–12165, doi:10.5194/acp-14- 12155-2014, 2014.

Pappalardo, G., Amodeo, A., Apituley, A., Comeron, A., Freudenthaler, V., Linné, H., Ansmann, A., Bösenberg, J., D'Amico, G., Mattis, I., Mona, L., Wandinger, U., Amiridis, V., AladosArboledas, L., Nicolae, D., and Wiegner, M.: EARLINET: towards an advanced sustainable European aerosol lidar network, Atmos. Meas. Tech., 7, 2389–2409, 10, http://www.atmos-meas-tech.net/7/2389/10/.5194/amt-7-2389- 2014, 2014.

Peterson, D. A., Campbell, J. R., Hyer, E. J., Fromm, M. D., Kablick, G. P., Cossuth, J. H., and DeLand, M. T.: Wildfire-driven thunderstorms cause a volcano-like stratospheric injection of smoke, Npj Climate and Atmospheric Science, 1, 30. https://doi.org/10.1038/s41612-018-0039-3, 2018.

Sicard M., Granados-Muñoz M.J., Alados-Arboledas L., Barragán R., Bedoya-Velásquez A.E., Benavent-Oltra J.A., Bortoli D., Comerón A., Córdoba-Jabonero C., Costa M.J., del Águila A., Fernández A.J., Guerrero-Rascado J.L., Jorba O., Molero F., Muñoz-Porcar C., Ortiz-Amezcua P., Papagiannopoulos N., Potes M., Pujadas M., Rocadenbosch F., Rodríguez-Gómez A., Román R., Salgado R., Salgueiro V., Sola Y., Yela M.: Ground/space, passive/active remote sensing observations coupled with particle dispersion modelling to understand the inter-continental transport of wildfire smoke plumes, Remote Sensing of Environment, 232, https://doi.org/10.1016/j.rse.2019.111294, 2019.

Sugimoto, N., Tatarov, B., Shimizu, A., Matsui, I., and Nishizawa, T.: Optical Characteristics of Forest-Fire Smoke Observed with Two-Wavelength Mie-Scattering Lidars and a HighSpectral-Resolution Lidar over Japan, SOLA, 6, 93–96, doi:10.2151/sola.2010-024, 2010.

Tesche, M., Ansmann, A., Müller, D., Althausen, D., Engelmann, R., Freudenthaler, V., and Groß, S.: Vertically resolved separation of dust and smoke over Cape Verde using multiwavelength Raman and polarization lidars during Saharan

Mineral Dust Experiment 2008, J. Geophys. Res., 114, D13202, doi:10.1029/2009jd011862, 2009.

Veselovskii I., Kolgotin, A., Griaznov, V., Müller, D., Wandinger, U., and Whiteman, D.: Inversion with regularization for the retrieval of tropospheric aerosol parameters from multi-wavelength lidar sounding, Appl. Opt., 41, 3685–699, https://doi.org/10.1364/AO.41.003685, 2002.

5   Veselovskii, I., Goloub, P., Podvin, T., Bovchaliuk, V., Derimian, Y., Augustin, P., Fourmentin, M., Tanre, D., Korenskiy, M., Whiteman, D. N., Diallo, A., Ndiaye, T., Kolgotin, A., and Dubovik, O.: Retrieval of optical and physical properties of African dust from multiwavelength Raman lidar measurements during the SHADOW campaign in Senegal, Atmos. Chem. Phys., 16, 7013–7028, https://doi.org/10.5194/acp-16-7013-2016, 2016.

Yu, P., Toon, O.B., Bardeen, C.G., Zhu, Y., Rosenlof, K.H., Portmann, R.W., Thornberry, T.D., Gao, R.-S., Davis, S.M.,
10   Wolf, E.T., de Gouw, J., Peterson, D.A., Fromm, M.D., and Robock, A.: Black carbon lofts wildfire smoke high into the stratosphere to form a persistent plume, Science, 365, 587-590, doi: 10.1126/science.aax1748, 2019.

Zhang, R., Khalizov, A. F., Pagels, J., Zhang, D., Xue, H., and McMurry, P. H.: Variability in morphology, hygroscopicity, and optical properties of soot aerosols during atmospheric processing, P. Natl. Acad. Sci. USA, 105, 10291–10296, https://doi.org/10.1073/pnas.0804860105, 2008.

30

Table 1. The parameters used for the generation of the look-up tables of the near – spherical particles.

Parameter	Range
$r_g(\mu m)$ [step]	0.1 – 0.7 [0.05]
σ_g (fixed)	0.4
m_r [step]	1.4 – 1.75 [0.05]
m_i [step]	0.005 – 0.045 [0.005]
ε_s [step]	0.6 – 1.55 [0.05]
σ_s (fixed)	0.05

5   **Table 2.** The parameters used for the generation of the look-up tables of the Chebyshev particles.

Parameter	Range
$r_g(\mu m)$[step]	0.1 – 0.7 [0.05]
σ_g (fixed)	0.4
m_r [step]	1.4 – 1.75 [0.05]
m_i [step]	0.005 – 0.045 [0.005]
u [step], T	- 0.15 – 0.15 [0.05], 4

Table 3. The parameters used for the generation of the look-up tables of the chain-like fractal aggregates.

Parameter	Range
R_v (µm)	0.5
R_m (µm)[step]	40 – 80 [20]
N_m	244, 579, 1953
D_f (fixed)	1.8
k_f (fixed)	1.3
m_r	1.4, 1.45, 1.5
m_i	0.005, 0.01, 0.03

5   **Table 4.** LR and PLDR layer-integrated mean values at 355, 532 and 1064 nm for the stratospheric smoke layer, on August 22, at Leipzig, Germany.

Parameter	355 nm	532 nm	1064 nm
PLDR (%)	22.4 ± 1.5	18.4 ± 0.6	4 ± 0.7
LR (sr)	40 ± 16	66 ± 12	92 ± 27

10   **Table 5.** The best fit of PLDR and LR at 355, 532 and 1064 nm, as calculated with the T-matrix code for near-spherical particles. The corresponding microphysical properties are shown in the first row. The relative differences with respect to the measured layer-integrated mean values are within the measurement errors shown in Table 4.

Solution: $k = 1.55 + i0.025$, $\varepsilon = 1.4$, $r_g = 0.25$µm			
	355 nm	532 nm	1064 nm
PLDR (%)	21.8	18.3	4.5
LR (sr)	41.7	64.2	98.5
PLDR rel. dif. (%)	2.8	0.6	12.5
LR rel. dif. (%)	4.3	2.7	7.1

Table 6. PLDR and LR at 355, 532 and 1064 nm, calculated with the T-matrix code considering Chebyshev particles for the microphysical properties shown in first row, and their relative difference with respect to the measured layer-integrated mean values. The relative differences that are highlighted in red, exceed the measurement errors of the layer-integrated mean values (Table 4).

	T4, $k = 1.5 + i0.02$, $u = 0.15$, $r_g = 0.3$ µm		
	355 nm	532 nm	1064 nm
PLDR (%)	23.1	16.5	3.5
LR (sr)	39.0	60.8	101.8
PLDR rel. dif. (%)	2.9	10.3	10.6
LR rel. dif. (%)	2.4	7.9	10.6

Table 7. Example values of PLDR and LR at 355, 532 and 1064 nm, calculated with the MTSM code for the microphysical properties shown in first row and first column, considering chain-like fractal aggregates shown in Fig. 2c. Their relative difference with respect to the measured layer-integrated mean values is also shown, while values in red are found to exceed the measurement errors of the layer-integrated mean values (Table 4).

	$R_m = 80$, $D_f = 1.8$, $k_f = 1.3$					
	PLDR			LR		
	355 nm	532 nm	1064 nm	355 nm	532 nm	1064 nm
Refractive index 1.4 + i0.03	7.4	3.6	0.8	86.2	77.9	82.6
Rel. dif. (%)	67.0	80.4	80.0	116.0	18.0	10.2
Refractive index 1.45 + i0.03	9.2	4.5	0.9	80.9	72.3	76.0
Rel. dif. (%)	58.9	75.5	77.5	102.3	9.5	17.4
Refractive index 1.5 +i0.03	11.3	5.4	1.2	77.3	67.5	71.1
Rel. dif. (%)	49.6	70.7	70	77.3	2.3	22.7
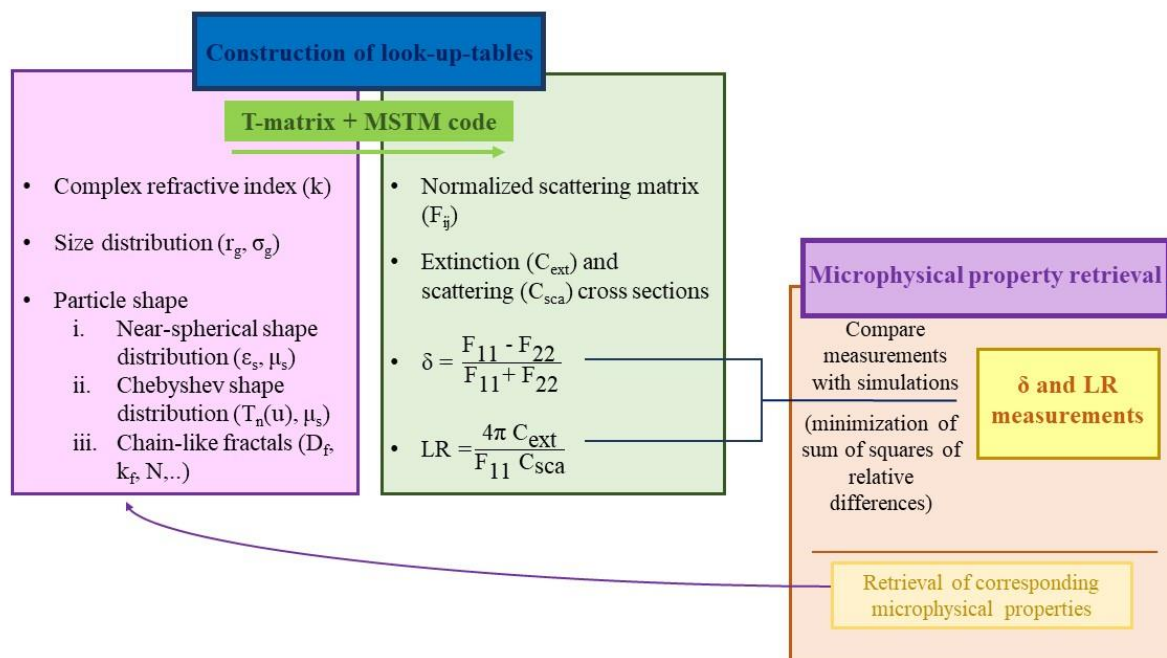
Figure 1. Overview of the methodology followed for establishing look-up-tables and the retrievals from T-matrix outputs.
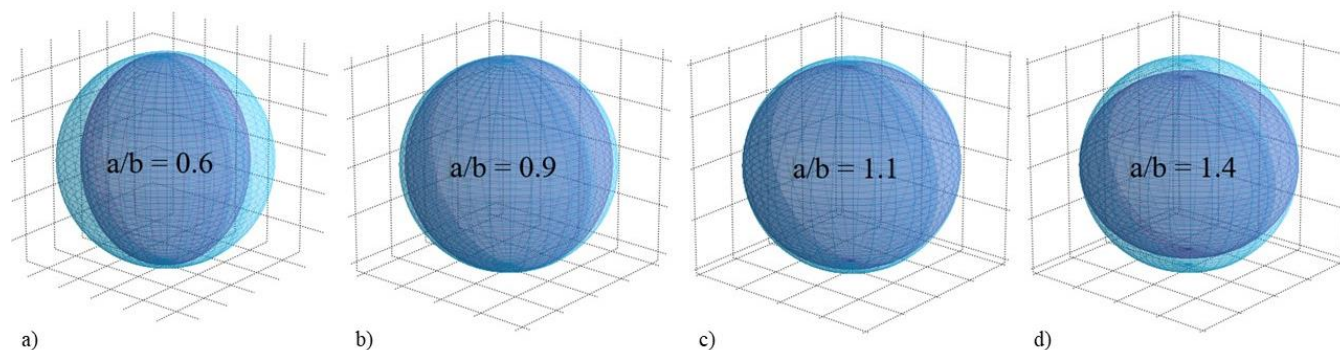
Figure 2: Examples of spheroids used (in grey colour), embedded in a perfectly spherical shell (in light blue colour), to visualize their deviation from the perfect sphere. From left to right: oblate spheroids with (**a**) $\varepsilon = 0.6$ and (**b**) $\varepsilon = 0.9$ and prolate spheroids with (**c**) $\varepsilon = 1.1$ and (**d**) $\varepsilon = 1.4$.

Figure 3: Fractal model morphologies composed of different number of monomers, used in MSTM code. For all fractals we use the same fixed value of fractal dimension D_f and fractal pre-factor k_f.

a)
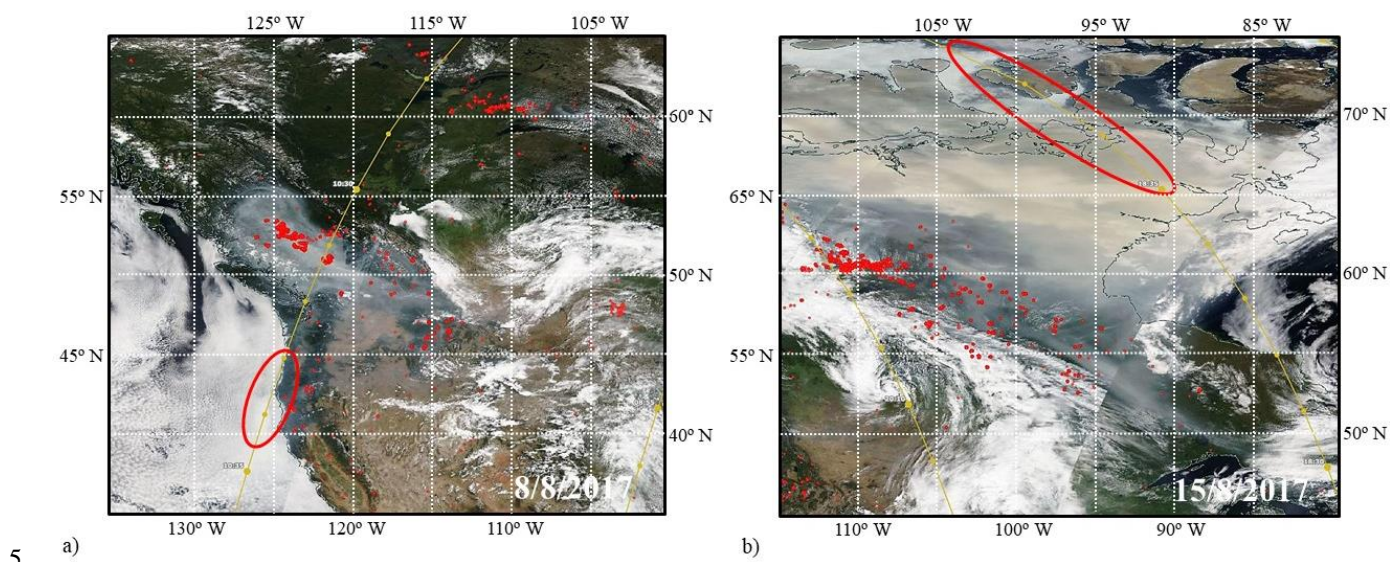
Figure 4: Corrected surface reflectance from MODIS, over-plotted with active fire regions and thermal anomalies (red dots) and CALIPSO ascending and descending overpasses (yellow lines). Red circles denote the position of the smoke plume on (a) August 8 2017 and (b) August 15 2017. Maps are generated from NASA Worldview Snapshots.
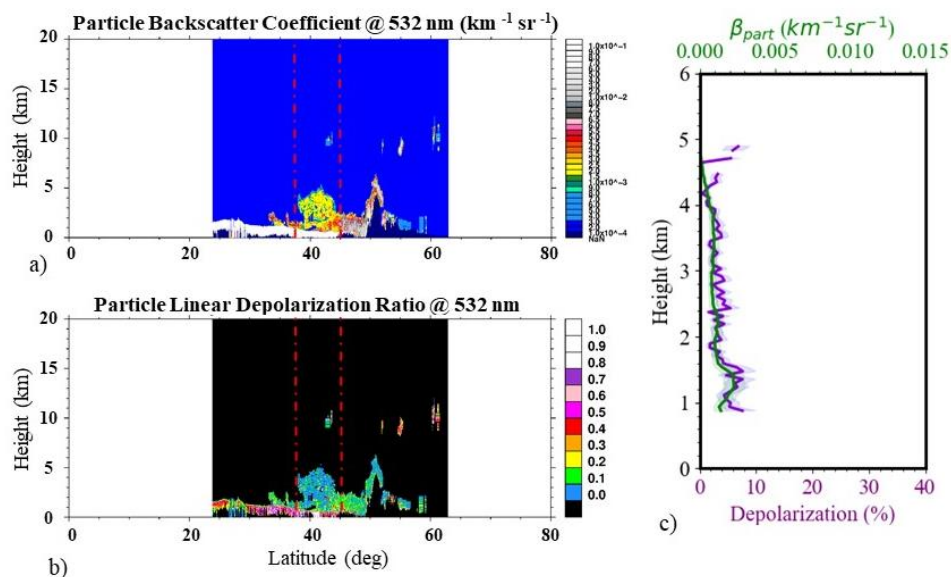
Figure 5: CALIPSO Backscatter Coefficient (km-1sr-1) and Particle Linear Depolarization Ratio (%) that correspond to the daytime overpass on 8/8/2017, 10:27 – 10:41 UTC shown in Fig. 4a. (a) The smoke plume is located between 39 and 45 ° latitude, below 6 km in altitude. Red dashed lines denote the spatial averaging applied for the retrieval of optical properties shown on the right plot. (b) PLDR values at 532 nm, do not exceed values of 3 – 4 %.
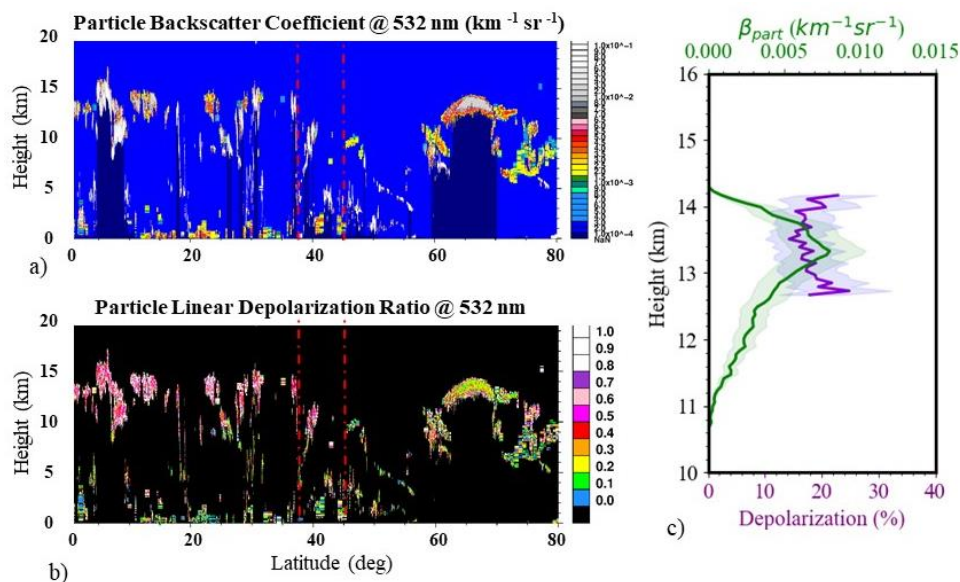
Figure 6: Same as Fig. 5 but for the night-time overpass of CALIPSO on 15/8/2017, 18:22 – 18:35 UTC shown in Fig.4b. (a) The smoke plume is now above the local tropopause at approximately 14 km, between 60 and 75 ° latitude. Red dashed lines denote the spatial averaging applied for the retrieval of optical properties shown on the right plot. (b) PLDR values at 532 nm (right plot, purple line) exceed 17%. (Note that the altitude range for this plot is from 10 to 16 km, whereas in Fig. 5b from 0 to 6 km).
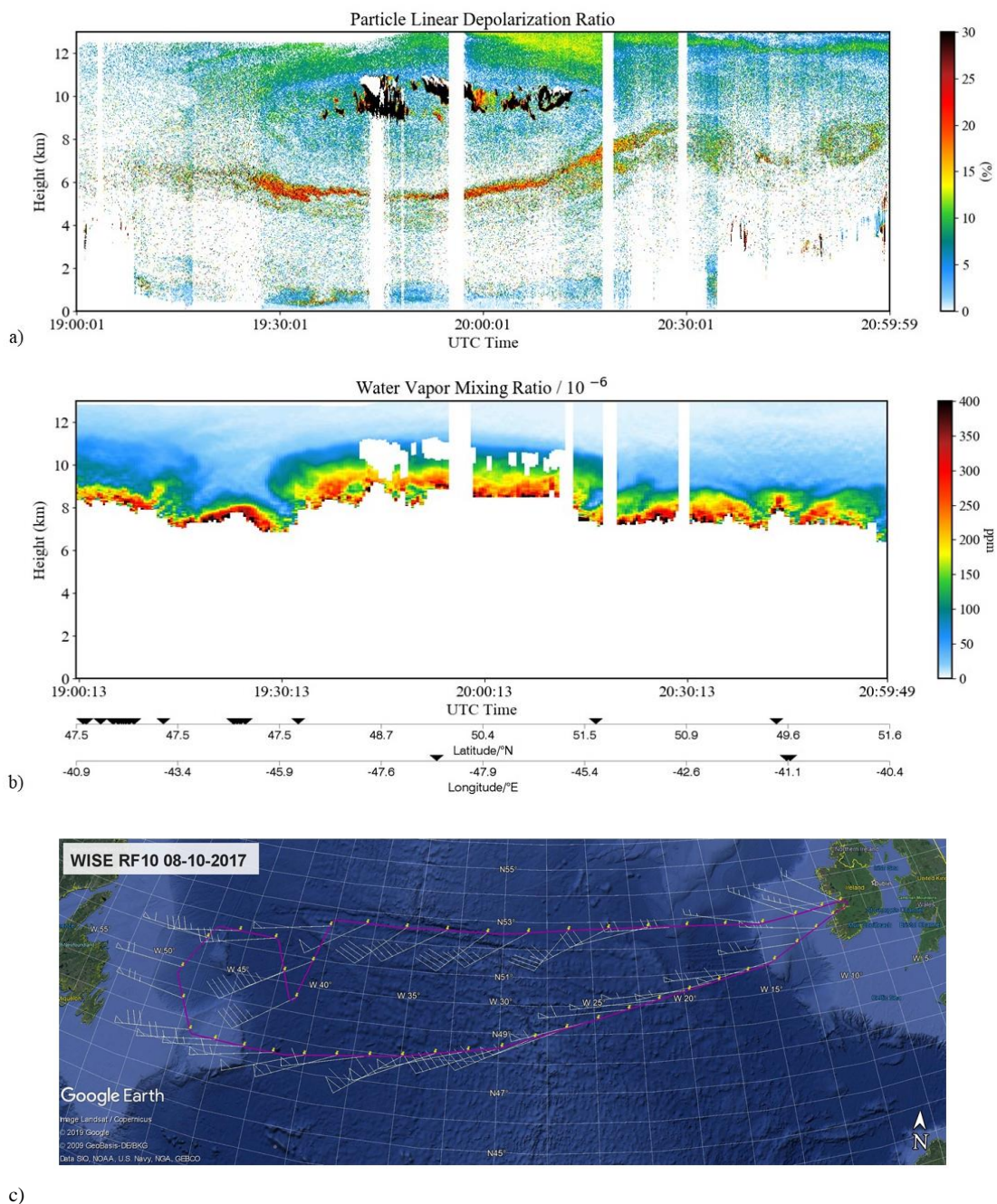
5 **Figure 7:** Time–height airborne lidar observations of the PLDR at 532 nm (a) and the Water Vapor Volume Mixing Ratio (b). Measurements were performed over the Atlantic Ocean, between 19:00 and 21:00 UTC on 7 October 2017 by the DLR HALO aircraft in the framework of WISE mission. The track of the aircraft is shown in (c) over-plotted on © Google Earth map.
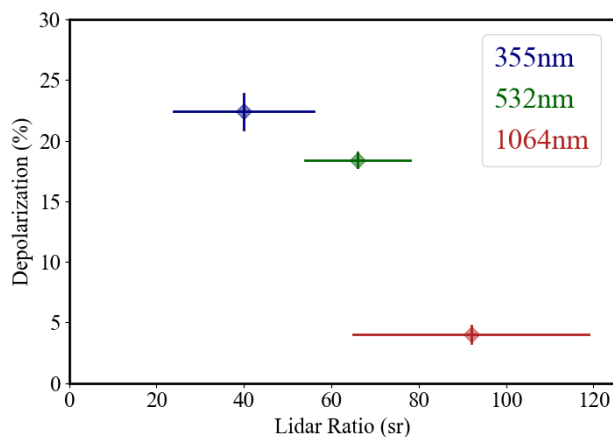
Figure 8: Intensive optical properties of the smoke particles found in the stratosphere, as measured on August 22, at Leipzig, Germany. The LR mean values are plotted against the PLDR mean values, along with the corresponding errors. A typically increasing behaviour of LR for aged Canadian smoke is observed at 355 and 532 nm, while for the PLDR the effect is the opposite: the surprisingly large, layer-integrated mean values drop from the UV to the Near-IR.
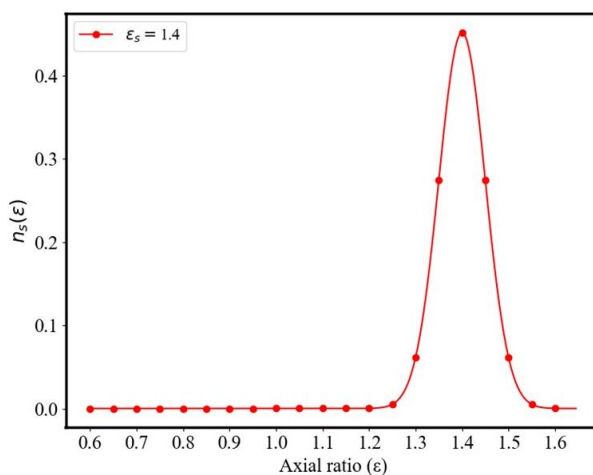
Figure 9. The retrieved axial-ratio distribution of the smoke particles assuming near-spherical shapes.
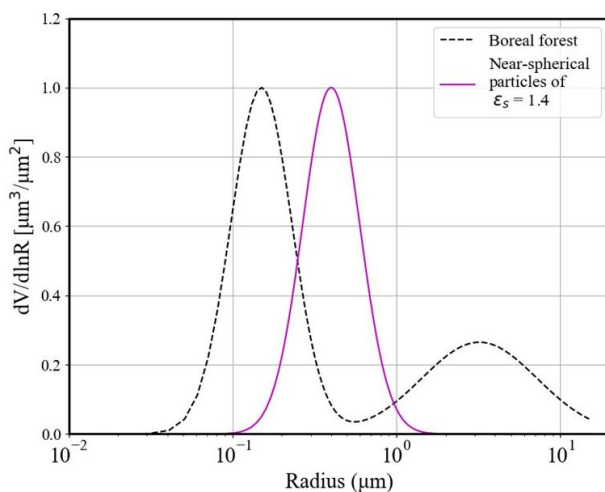
Figure 10. Typical AERONET size distribution for biomass burning (black dash line) (Dubovik et al., 2002), and the retrieved size distribution for near-spherical smoke particles (pink line). Both are normalized to their maximum value.
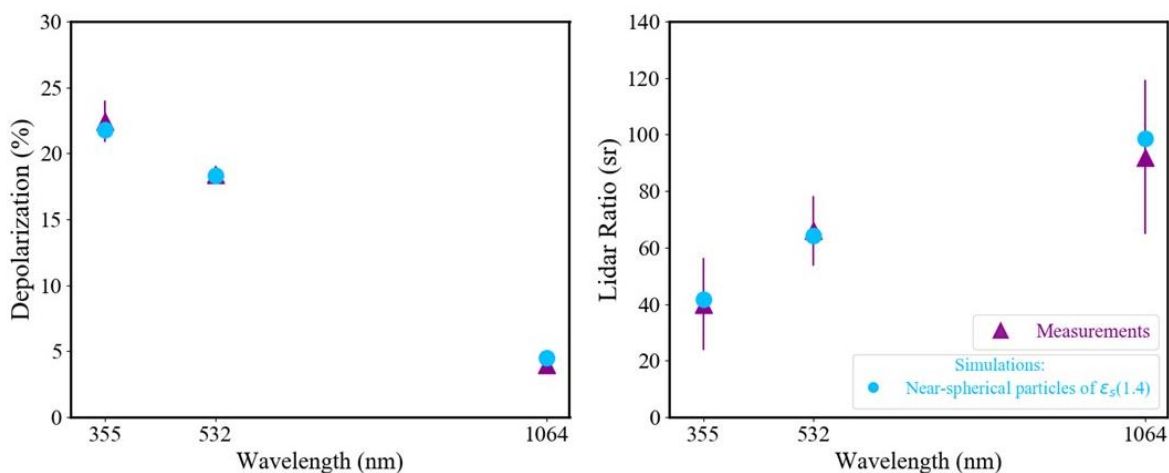
Figure 11: The fitting of measured PLDR (a) and LR (b) at 355, 532 and 1064 nm, with T-matrix simulations considering near-spherical particles. Purple triangles correspond to measurements on August 22, at Leipzig, Germany, while blue circles to simulations assuming near-spherical particles of mean axial ratio ε_s = 1.4, mean geometric radius r_g = 0.25μm and a wavelength independent complex refractive index k = 1.55 + i0.025.
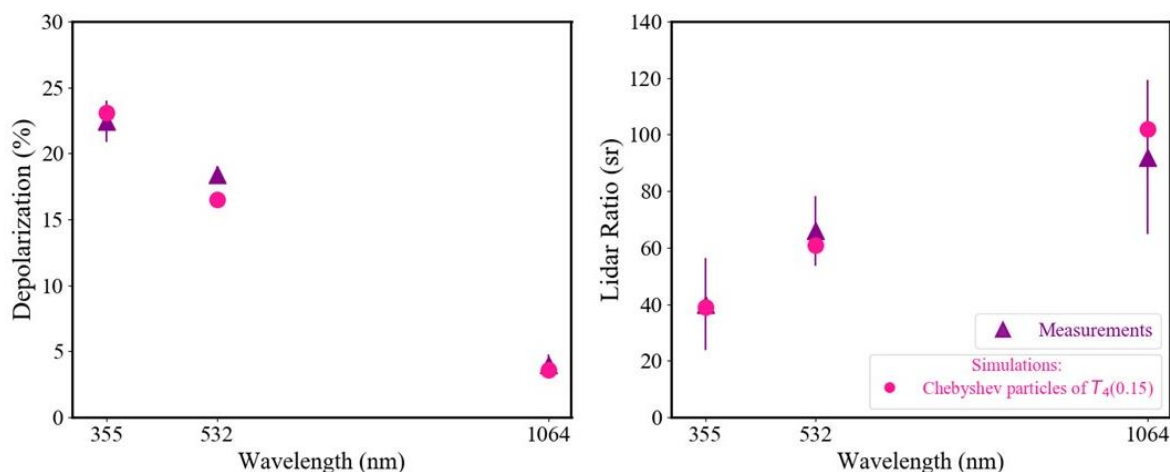
Figure 12: The fitting of the measured PLDR (a) and LR (b) at 355, 532 and 1064 nm, with T-matrix simulations considering Chebyshev particles. Purple triangles correspond to measurements on August 22, above Leipzig, Germany, while pink circles to simulations assuming Chebyshev particles of fourth degree.
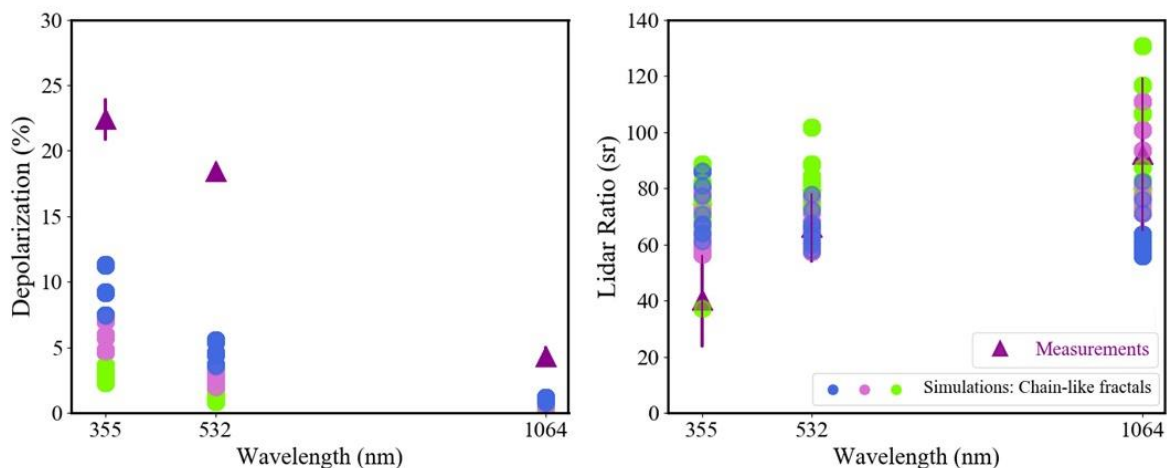
Figure 13: Fitting of the measured PLDR (a) and LR (b) at 355, 532 and 1064 nm, with MSTM simulations considering chain-like fractal aggregates. Purple triangles correspond to measurements on August 22, at Leipzig, Germany, while green (monomer radius $R_m = 40\mu m$), pink (monomer radius $R_m = 60\mu m$) and blue (monomer radius $R_m = 80\mu m$) circles correspond to simulation results for the chain-like fractal
10 aggregates shown in Fig. 3 with of $D_f = 1.8$ and $k_f = 1.3$.
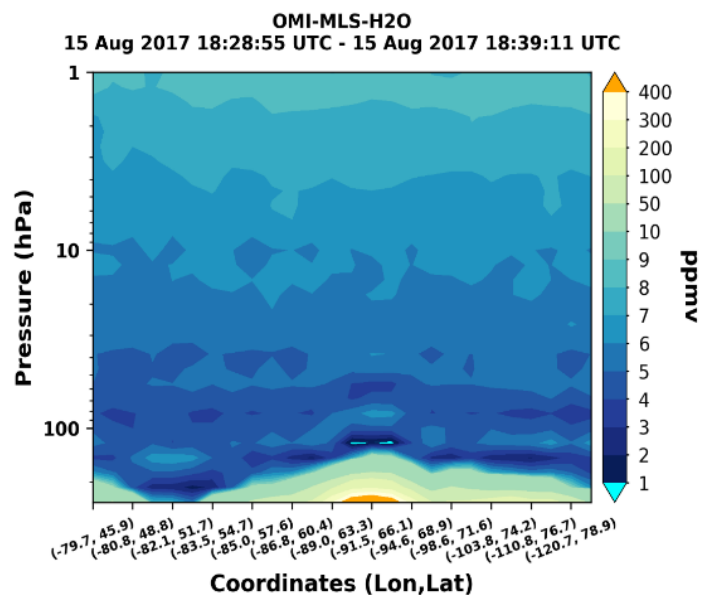
Figure 14: MLS water vapour measurements for a night-time overpass on August 15, 2007 (see also Fig. 3b from MODIS). A positive water vapour anomaly is observed at 200hPa (Yu et al., 2019).

(a)

(b)
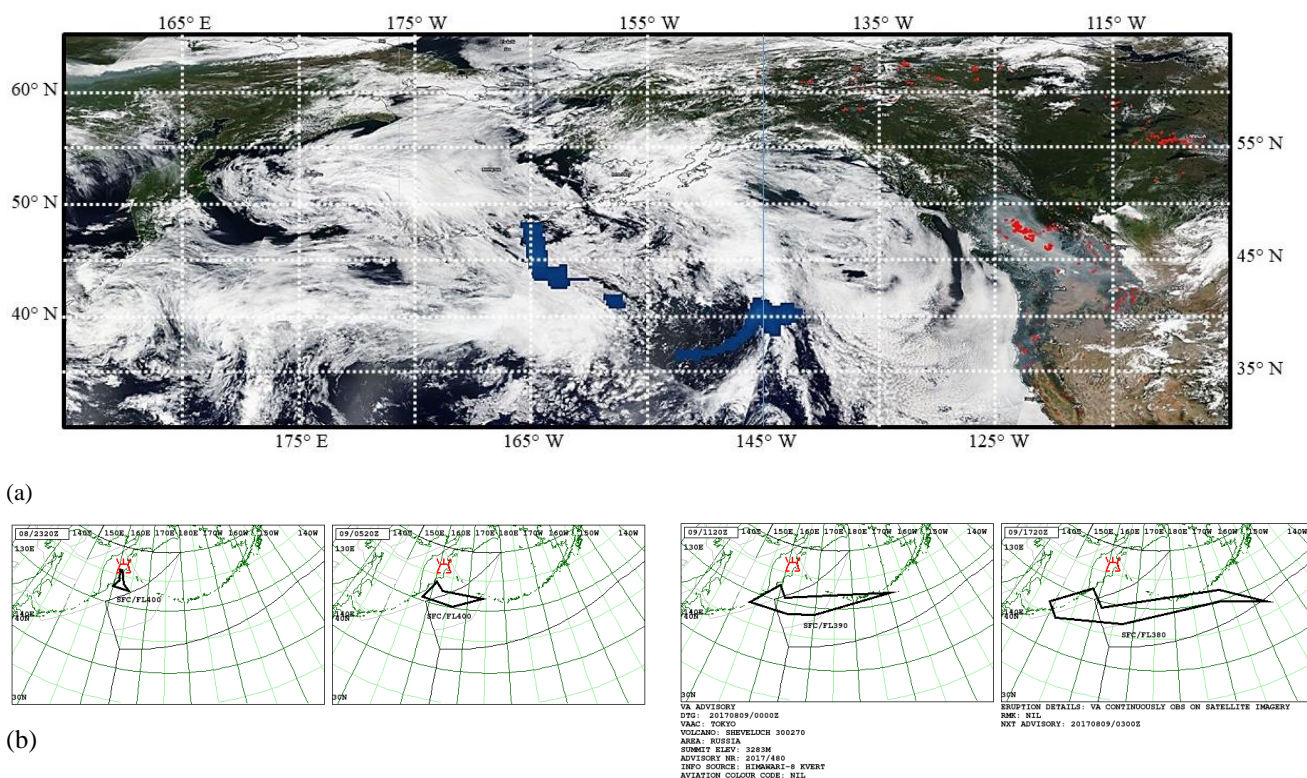
Figure 15: MODIS true colour image (a) on 8 August 2017, overlaid with sulphur dioxide concentration in middle and upper troposphere product from Suomi NPP (blue colour) and (b) satellite images from HIMAWARI-8 on the same day (source: Tokyo Volcanic Advisory Centre (Tokyo VAAC)). In both figures we can identify the plume that moves south-easterly towards the area of British Columbia.